ACS SENSORS

pubs.acs.org/acssensors

Article

Enhanced Microfluidic Sample Homogeneity and Improved Antibody-Based Assay Kinetics Due to Magnetic Mixing

Eriola-Sophia Shanko, Lennard Ceelen, Ye Wang, Yoeri van de Burgt, and Jaap den Toonder*

Cite This: *ACS Sens.* 2021, 6, 2553–2562

Read Online

ACCESS | Metrics & More | Article Recommendations | Supporting Information

ABSTRACT: Recent global events have distinctly demonstrated the need for fast diagnostic analysis of targets in a liquid sample. However, microfluidic lab-on-a-chip devices for point-of-care diagnostics can suffer from slow analysis due to poor mixing. Here, we experimentally explore the mixing effect within a microfluidic chamber, as obtained from superparamagnetic beads exposed to an out-of-plane (vertical) rotating magnetic field. Various magnetic protocols are explored, and the level of sample homogeneity is measured by determining the mixing efficiency index. In particular, we introduce a method to induce effective mixing in a microfluidic chamber by the actuation of the same beads to perform global swarming behavior, a collective motion of a large number of individual entities often seen in nature. The microparticle swarming induces high fluid velocities in initially stagnant fluids, and it can be externally controlled. The method is pilot-tested using a point-of-care test featuring a bioluminescent assay for the detection of antibodies. The mixing by the magnetic beads leads to increased assay kinetics, which indeed reduces the time to sensor readout substantially. Magnetic microparticle swarming is expected to be beneficial for a wide variety of point-of-care devices, where fast homogeneity of reagents does play a role.

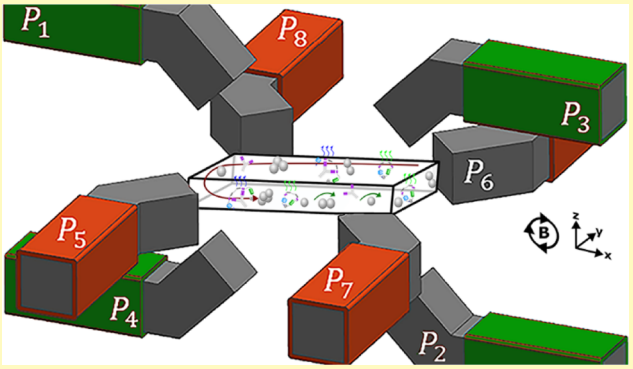

KEYWORDS: *microfluidics, swarming, micromixing, superparamagnetic beads, antibody testing*

The novel coronavirus has been a perfect example to highlight the importance of rapid diagnostic testing since it crucially facilitates quick identification of cases, fast treatment for the infected, and immediate isolation to prevent spread.[1] Within a short amount of time, the coronavirus spread all across the globe, resulting in societies to almost completely shut down. It is thus essential to develop rapid diagnostic tools that would enable fast identification of infections and subsequently fast decision making. Fast analysis does not apply only to the novel coronavirus but to every emerging infectious disease or in general, analyte testing where time is of pivotal importance. Lab-on-chip devices have received widespread attention as diagnostic tools because of their wide applicability to bio(chemical) processes while taking advantage of favorable features such as small sample volume requirements, fast analysis, small device sizing, ensuring accessibility to remote areas and high-throughput capabilities. Point-of-care (PoC) devices utilize lab-on-chip technologies to deliver testing results at the PoC in a fast turnaround time. Recent examples of lab-on-chip (bio)chemical processes are antibody (AB)-based testing such as the SARS-CoV-2 tests,[2] bacteria detection,[3] cancer cell isolation,[4] biomarker detection for the identification of different diseases,[5] with broad applications in water quality measurements,[6] cancer diagnostics,[7] drug administration,[8] and more, that could translate into a PoC device.

PoC devices also bring a major challenge, namely, the need for device user-friendliness. To ensure this requirement, usually the components necessary for the analysis (e.g., the biosensor) are already incorporated inside the microfluidic device. This can be done via deposition methods. Fast analyte capturing detection requires (1) fast spreading of the deposited biosensor in the liquid sample (Figure 1a) and (2) fast binding events of the target and the biosensor in the matrix (Figure 1b).

To be successful, PoC readouts need to be accurate and reproducible, with high sensitivity and specificity. The efficiency and reproducibility of capturing and detection of targets is strongly dependent on the global homogeneity of the reagents within the complete sample volume.[9] A means to achieve homogeneity is to enhance fluid mixing which will help

Received: January 8, 2021
Accepted: June 15, 2021
Published: June 30, 2021

https://doi.org/10.1021/acssensors.1c00050
ACS Sens. 2021, 6, 2553–2562

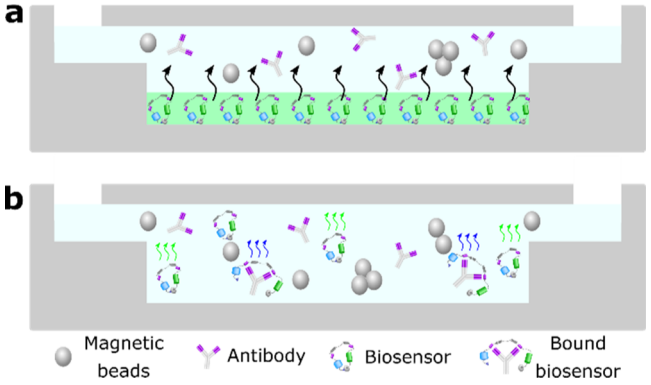

Figure 1. Need for efficient mixing in lab-on-chip devices. (a) Magnetic beads can increase the effective diffusivity and hence the spreading of a deposited AB-based biosensing array in a microfluidic chip and (b) magnetic beads can increase the binding events between a target (here, AB biosensor).

to overcome limitations at the microscale imposed by timescales of molecular diffusion. However, mixing in microfluidics is challenging due to the low Reynolds numbers.[10]

One solution to overcome these challenges involves the incorporation of passive geometrical structures, which induce specific flow patterns that eventually lead to mixing. However, these structures are difficult to adjust upon fabrication and require long mixing lengths. Moreover, in stagnant fluids such as those often present in microreaction chambers in PoC devices, passive mixing structures do not work since they require externally driven flow. On the other hand, active means of mixing (e.g., acoustic and magnetic) provide controllable and more efficient mixing in capillary, low-Reynolds number ($Re \ll 1$) microfluidics. However, active micromixers can be complex and costly to fabricate, particularly due to their need for external components.[11] Magnetic microparticle mixing offsets complex fabrication and reduces cost because actuation is done remotely without physical connection to the device. Furthermore, magnetic microparticles are commercially available, often already used for target capturing and separation without active mixing and can be externally controlled via electromagnets. Magnetic microparticles have been studied to sort, transport, and capture targets in a microfluidic chip. Here, we exploit an additional function of these magnetic capturing elements that increase fluid kinetics and subsequently sample homogeneity via mixing.

It has been demonstrated that an external magnetic field can induce self-assembly of suspended magnetic beads into (anisotropic) chains as a result of the dipole−dipole interactions between the beads.[12] When these chains are subjected to a rotating magnetic field, they evoke a rotational motion, which locally stirs and mixes the fluid (microstirrers).[13] Under certain conditions, a phenomenon of collective motion of these microstirrers occurs, which can induce strong vortical flow in a microfluidic chamber.[14]

Here, we present a magnetic actuation configuration and associated protocols that lead to a phenomenon in a microfluidic chamber, which we call "magnetic particle swarming" (MPS) due to its resemblance to bird swarming. Due to this phenomenon, magnetic bead chains do not only exhibit local rotational motions to cause local vortices but also a global rotational motion throughout the microchamber, which is important for reaching global sample homogeneity. The microfluidic mixing induced by the MPS shows potential for enhanced micromixing for fast PoC testing, in particular for no-flow-through systems in which mixing must be achieved in initially stagnant fluids. Therefore, we analyze the MPS in depth: we systematically study the occurrence of MPS in relation to two of the most determinant parameters for its formation, namely magnetic field rotational frequency and magnetic field strength. We study the resulting bead dynamics, quantify the induced fluid flow, as well as the resulting mixing effectiveness (i.e., the level of solution homogeneity). The analysis shows how the phenomenon depends on the relative importance of magnetic and viscous forces at work. Finally, we demonstrate the effect of magnetic mixing induced by MPS on a bioluminescent AB-based sensor assay for PoC applications in terms of time to readout.

MAGNETIC BEAD BEHAVIOR IN VARIOUS MAGNETIC PROTOCOLS

Homogeneity of reagents within a microfluidic chip has proven to be beneficial for the efficient capturing of elements and the reproducibility of testing. Fluid/reagent homogeneity, or mixture quality, is thus crucial.

Two key elements are required to achieve enhanced mixing in microfluidic devices utilizing MPS: magnetic beads and a time-dependent magnetic field that controls these magnetic beads (for details, see the Supporting Information Text S1 "Materials and Methods"). Time-dependent magnetic fields, such as we apply here, can be generated by rotating or translating permanent magnets but achieving a relatively uniform field and relatively high rotation rates (as we need here) will be difficult in practice and requires a rather bulky setup.[15] Electromagnets are preferred for PoC as the magnetic field is easily controlled both in terms of spatial field distribution and time dependency, they can be made small, and no moving parts are incorporated, which would require follow-up maintenance. A custom-built electromagnetic setup is used to generate the magnetic field; see Figure 2a.[16] Poles P1−P4 can generate a magnetic field in the vertical plane and poles P5−P8 in the horizontal plane; by combining them, 3D manipulation of the magnetic beads (Figure 2c(2−3)) is

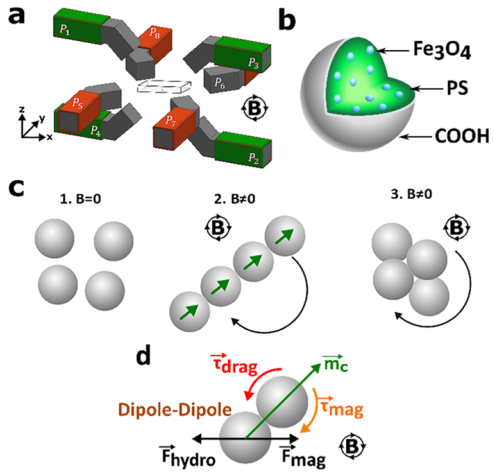

Figure 2. Key ingredients for magnetic mixing. (a) Octopolar electromagnetic setup. Only the four vertical poles are actuated (green, P1−P4) to induce a vertical rotational magnetic field. (b) Structure of the used magnetic beads, (c) overall behavior of magnetic beads in the absence and presence of the magnetic field, and (d) forces acting on a two-bead chain in a rotating field.

https://doi.org/10.1021/acssensors.1c00050
ACS Sens. 2021, 6, 2553−2562

possible. In this research, only the four poles in the vertical plane are used to generate an out-of-plane rotating magnetic field relative to a microfluidic chamber (Figure 2a). The two pairs of poles are actuated in a sinusoidal waveform with a 90° phase difference; therefore, combined, a rotational field is generated. The amplitude of the field and the frequency are adjusted using a LabView platform. These values correspond to various generated magnetic field strengths and rotational frequencies.

The magnetic beads of choice are of superparamagnetic nature owing to their sensitivity to magnetic field changes. These superparamagnetic iron-oxide microparticles (SPIOMs) consist of many separate monodomain iron-oxide nanoparticles incorporated inside a polymer matrix (Figure 2b). The SPIOMs ($\varnothing$ = 10 μm, micromer-M, micromod, ~6000 beads μL^{-1}) used are coated with (negatively charged) carboxylic groups to prevent agglomeration. These are the same magnetic beads with similar concentration as in previous work,[14] where strong flows were reported.

In the absence of a magnetic field, the nanoparticles feature random magnetic dipole directions, the beads have zero net magnetization, and they do not interact magnetically (Figure 2c1). In the presence of a magnetic field with flux density $\vec{B}$, the nanomagnetic dipoles align to the magnetic field lines and the magnetic particles obtain a net magnetic dipole moment $\vec{m}_p = V_p \chi_p \vec{B} \mu_0^{-1}$ where V_p is the particle volume, χ_p is effective magnetic particle susceptibility, and μ_0 is the magnetic permeability of free space, which equals $4\pi \times 10^{-7}$ NA^{-2}, which causes the magnetic particles to chain up due to dipolar interactions (Figure 2c(2)).

When the magnetic field becomes rotational, the chains start rotating. The chains remain straight and intact and rotate with the field at low frequencies (<10 Hz) for the specific particles and experimental conditions used in this study. At higher frequencies, the long chains break up to form either two-particle chains or clusters (Figure 2c3) due to the higher hydrodynamic drag acting on the particles. Finally, when the rotating magnetic fields are such that hydrodynamic, viscous, and magnetic forces strike the right balance, a global, rather than local, motion of the beads is observed that results in swarming and a global fluid motion and ultimately in enhanced mixing, as we will see later.

The various forces and torques acting on the SPIOMs with radius R, suspended in a fluid with viscosity η, are presented in Figure 2d. The main forces are the magnetic force due to the gradient of the magnetic field $\vec{F}_{mag} = (\vec{m}_p \cdot \vec{\nabla})\vec{B} = (V_p \chi_p \mu_0^{-1})(\vec{B} \cdot \vec{\nabla})\vec{B}$ and the hydrodynamic drag $\vec{F}_{hydro} = -6\pi\eta R\vec{U}$ due to the translation of the SPIOM in the fluid, where $\vec{U}$ is the particle velocity relative to the fluid. In addition, dipolar magnetic forces[17] result in magnetic particle−particle interactions and possible magnetic bead chain and cluster formation (see Supporting Information Text S1). Other (interparticle) forces such as electrostatic and van der Waals forces play a negligible role compared the magnetic and viscous effects for the particles we use.

Magnetic beads in a chain exhibit anisotropy, with a net dipole moment ($\vec{m}_c$) in the direction of the long-chain axis (Figure 2d). When the magnetic field becomes rotational, a magnetic torque $\vec{\tau}_{mag} = \vec{m}_c \times \vec{B}$ occurs that tends to align the chain to the magnetic field $\vec{B}$ (see Supporting Information Text S2); this is also the mechanism of magnetic-bead chain rotation and subsequent local mixing.[18] A viscous drag torque $\vec{\tau}_{drag}$ (see Supporting Information Text S2) counteracts the $\vec{\tau}_{mag}$, causing the magnetic bead chains to rotate at a phase lag compared to the applied magnetic field rotation. In addition, the moving particles interact hydrodynamically: the fluid flow generated by one particle can affect the motion of all other particles. Boundary restrictions due to the geometrical confinement of the microchamber also play an important role. All these magnetic and hydrodynamic forces are interdependent and the way in which they are balanced completely determines the dynamics of the magnetic microparticle motion and the induced fluid flow. The result can be controlled by adjusting the magnetic field frequency and amplitude, as well as the liquid viscosity, as is apparent from the dependency of the forces and torques on these parameters. Thus, in our experiments we concentrate on the magnetic field amplitude and frequency and explore the influence of changing these parameters on the (collective) particle motion, induced fluid flow, and mixing. We quantitatively analyze the results in terms of their Mason number dependency. The Mason number Ma, represents the ratio of viscous to magnetic forces acting on the beads and is defined as $Ma = 16\mu_0\eta\omega/\chi^2B^2$, where $\eta = 1 \times 10^{-3}$ Pa·s is the viscosity of the surrounding fluid, ω is the angular velocity of the magnetic field, χ is the dimensionless susceptibility of the beads, which was measured to be 0.04 (see Supporting Information Text S1) and it relates to the effective magnetic susceptibility χ_p by $\chi/(1 + \chi/3)$, and B is the applied magnetic flux density.[19] Ma has been applied to explain the dynamics of particle chains rotating in a viscous fluid.[20] At low Ma, magnetic forces dominate, and magnetic bead chains remain intact and may generate substantial (local) flow and mixing. At high Ma, viscous drag forces dominate, leading to chain breakup and lower local flows and less mixing.

The experiments are performed in a closed rectangular microfluidic chamber (4 × 4 mm and 500 μm high, see Supporting Information Text S1 for details). A clockwise rotational vertical magnetic field with a magnetic field strength of 25 mT is chosen to study the effect of rotational frequency on collective magnetic bead motion, that is, the field rotates in the xz-plane in Figure 2a. The applied frequency ranges from 1 to 60 Hz. The results are presented in Figure 3 as top-down images of the microfluidic chamber (i.e., showing the xy-plane) and in Supporting Information Movies S3.1−S3.4. Different types of collective magnetic particle behavior are observed.

At time zero, the magnetic microparticles have settled on the bottom of the chamber. In all cases, an initial global collective attraction toward the central band and to the right of the chamber is observed within the first 10 s of magnetic actuation, as is clearly visible in Supporting Information Movies S3.1−S3.4. At certain frequencies (>10 and <60 Hz) and after 60−90 s, a collective behavior of the particles, chains, and clusters in the form of a global circulatory motion in the microfluidic chamber is observed. The dipolar interactions of some clusters do not seem to be strong enough to endure the hydrodynamic torques, and within 3 min, most of the clusters break up into smaller rotating chains while gradually forming and maintaining a 1.5 mm wide band with stable and global collective circulatory motion in the central area of the chamber.

The global circulation is counterclockwise: in Figure 3, toward the left near the top of the chamber and toward the right near the bottom, opposite to the applied rotating magnetic field. Within the band, particle chains and clusters continuously rotate clockwise (in the rotation direction of the field), break up, and reform in a dynamic fashion. This resembles the swarming often observed in nature, by flocks of

https://doi.org/10.1021/acssensors.1c00050
ACS Sens. 2021, 6, 2553−2562

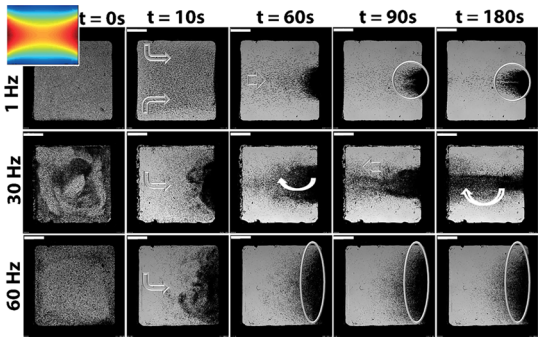

Figure 3. Collective SPIOM motion at 25 mT vertical magnetic rotation (only the four vertical poles—P1−4 (Figure 2a)—are actuated) at different rotation frequencies and at different time points in a 3 min vertical magnetic rotation protocol. The images are snapshots at different times in a top view of the 4 × 4 mm microfluidic chamber (i.e., the *xy*-plane in Figure 2a). The arrows indicate SPIOM motion, while the circles depict the positions of concentrated collections of the SPIOM. The insert at the top left shows the time-averaged magnitude of the magnetic field over one rotational cycle over the entire chamber at $z = 0$, obtained by computer simulations—red = high and blue = low field [14], reproduced by permission of The Royal Society of Chemistry. MPS is observed at actuation frequencies between 20 and 50 Hz, here visible in the 30 Hz results. Scale bar is 1 mm. Supporting Information Movies S3.1−S3.4 correspond to these experiments.

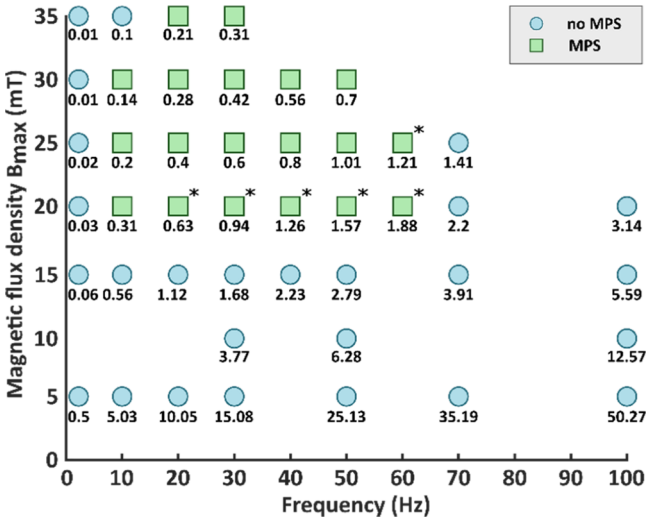

Figure 4. Frequency, magnetic field strength dependencies of magnetic bead dynamic behavior. The corresponding Mason numbers are also indicated. Only at a magnetic field strength of at least 20 mT, frequencies between 10 and 60 Hz, and $0.1 < Ma < 2$, MPS is observed. The stars (*) indicate conditions at which the magnetic bead dynamic behavior is not always reproducible.

birds and schools of fish, and therefore, we call this phenomenon MPS. Supporting Information Movie S3.3 shows this behavior. However, at frequencies <10 and >60 Hz, all particles drawn to the side of the chamber initially remain in place and form a dense collection ("island") of beads even though they exhibit individual (and local) dynamic motion.

MPS only occurs within a certain range of frequencies and *Ma* numbers in these experiments. Additional experiments where the magnetic field strength was varied were also performed to quantitatively analyze potential dependencies of MPS on the magnetic field strength. We calculated *Ma* for all applied flux densities (5−35 mT) and magnetic field angular frequencies (1−100 Hz). All results are summarized in Figure 4. Indeed, MPS is observed at a range of magnetic field strengths above 20 mT, frequencies between 10 and 60 Hz, and Mason numbers in the range $0.1 < Ma < 2$. Some of the above observations include additional motion of the magnetic beads such as pulsatile behavior (see Supporting Information Movie S3.1 and sometimes seen in S3.2).

GENERATION OF MPS

Given that the swarming is a collective global motion of the magnetic beads, it is expected to benefit global mixing and thus global homogeneity within the microreaction chamber with initially stagnant fluids. To better control this phenomenon, an in-depth analysis of why swarming occurs is executed. All the results suggest that swarming occurs only when a specific balanced combination of forces and torques is exerted onto the magnetic beads. In addition, the geometrical confinement plays an important role in the swarming formation (below Figure 5).

It is hypothesized that swarming is enabled by the following mechanism; see Figure 5. Before actuation starts, the magnetic particles are uniformly distributed on the microreaction chamber floor Figure 5).

1. Initialization: upon starting the actuation, chains and clusters are formed due to induced dipolar magnetic forces, and these begin to rotate with the field due to the magnetic torque $\vec{\tau}_{mag}$. This, in turn, creates fluid flow that interacts with the particles. In addition, rotating particle chains and clusters interact with the chamber floor, resulting in net translation of the particles to the right of the chamber (Figure 5). The insert in Figure 3 shows that the average magnetic field within the chamber is not uniformly distributed. The magnetic gradient force $\vec{F}_{mag}$ is expected to act on the particles, driving them to the central band and to enhance attraction to the (right) edge of the chamber toward the magnetic poles present there.
2. Island formation: after the initial formation of the central band, a densified island of dynamically moving magnetic particles at the right chamber edge occurs (Figure 5). The main mechanisms behind dynamic densifications forming the vortices have been characterized previously.[21] However, in contrast to that study, our global vortex (MPS) is highly influenced by the geometrical restrictions imposed by the microfluidic chamber. For the first 30 s, most of the magnetic beads remain in the island. However, at 20−50 Hz and magnetic field strengths over 20 mT, some magnetic bead chains are seemingly ejected from the core of the swarm (similar to (ref 22)) toward the center of the chamber, and most of the clusters break up to form chains or smaller clusters when in contact with the geometrical restriction of the chamber walls (Figure 5). In low magnetic field strength and low frequencies, the magnetic torque $\vec{\tau}_{mag}$ hinders the formation of the MPS. In addition, the resulting particle and fluid motion are too weak to overcome the magnetic gradient force $\vec{F}_{mag}$ that attracts the beads toward the edge, caused by the presence of the poles to the side (see the insert of Figure 3). The insert shows the presence of the higher field at the chamber edge, and this results in the particles remaining trapped in the

https://doi.org/10.1021/acssensors.1c00050
ACS Sens. 2021, 6, 2553−2562

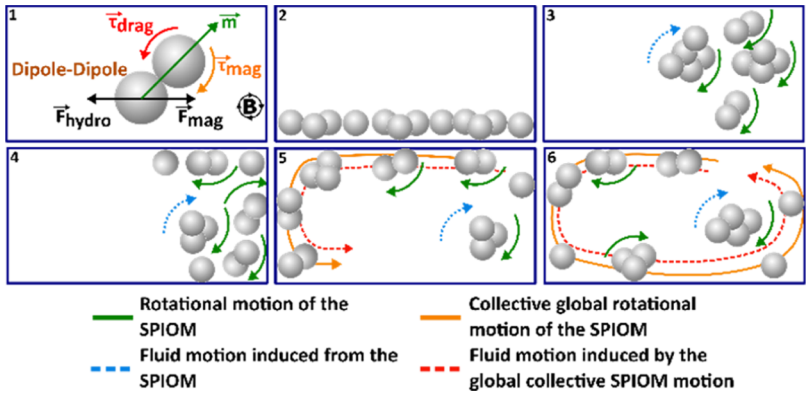

Figure 5. Acting forces and torques on two magnetic beads forming a chain and the sequence of events leading up to MPS. The motion of the superparamagnetic iron oxide magnetic bead chains and clusters (SPIOM) motion and the induced local and global flows are also portrayed. It is noted that other than the forces and torques acting on the magnetic beads, the geometrical restriction also plays an important role. The schematics are not to scale, and the blue squares indicate the geometry of the chamber.

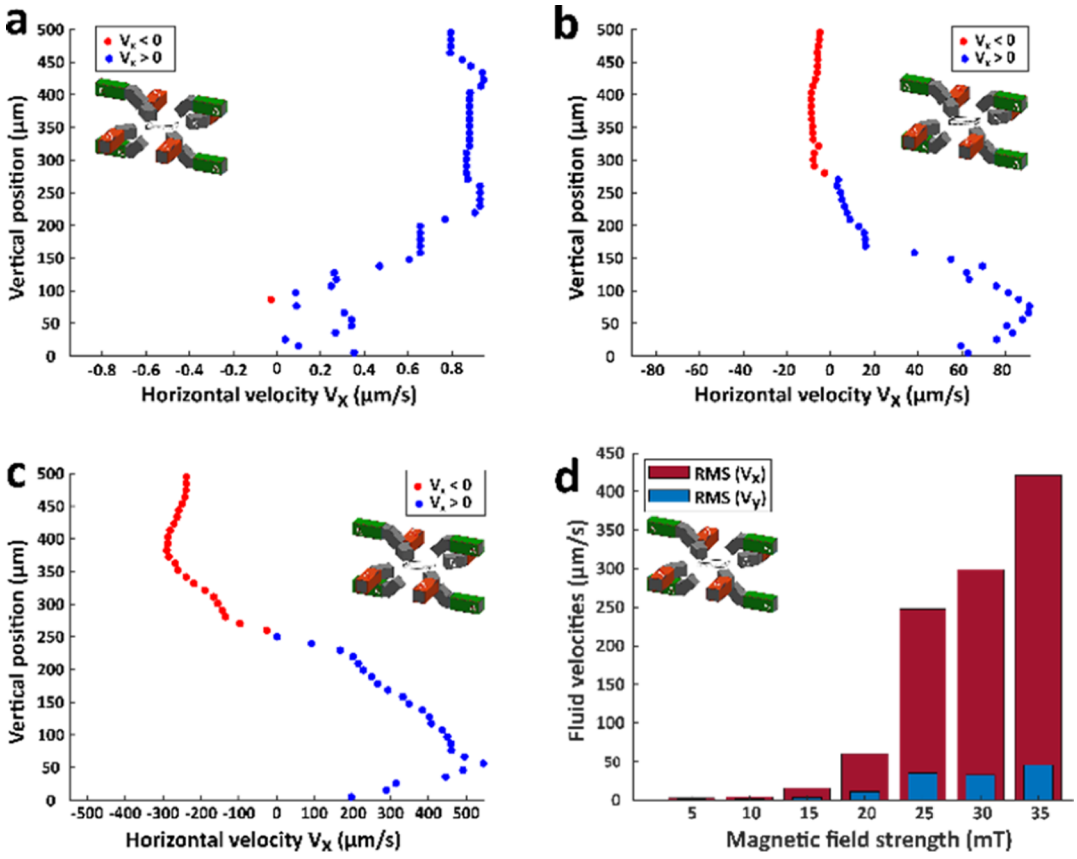

Figure 6. (a−c) Mean velocity profiles obtained from 3D-PTV measurements as a function of the vertical position in the chamber, from bottom (z = 0) to top (z = 500 μm). The averages are based on measurements in the central part of the chamber, that is, 1.3 < x < 2.7 mm and 1.3 < y < 2.7 mm. (a) No actuation, (b) actuation with 30 Hz, 15 mT (no MPS observed), and (c) actuation with 30 Hz, 35 mT (MPS observed). The color of each marker is defined by sign of the horizontal velocity V_x. There is a clear bias for a positive horizontal velocity near the bottom and for a negative horizontal velocity near the top of the fluid chamber, especially for the MPS case. (d) rms of the V_x and V_y, which correspond to the fluid velocities in the x and the y directions at different magnetic field strengths at 30 Hz applied rotational frequency.

island. On the other hand, for high frequencies, the viscous drag torque $\vec{\tau}_{drag}$ becomes so large that even the smallest clusters and chains break up. This in turn results in individual particles with only small or no magnetic torque and resulting fluid motion, making it again difficult for the particles to escape toward the chamber center against the magnetic gradient force acting toward the edge, and thus, the island stays intact.

3. MPS: In the development of MPS, the rotating particle chains and clusters that escape from the island start interacting with the top wall of the chamber; see Figure 5. In an applied clockwise rotating magnetic field, the chains and clusters also rotate clockwise and when close to the chamber wall, this angular momentum is converted into a translational motion as shown in the figure, when the magnetic chains and clusters tumble

https://doi.org/10.1021/acssensors.1c00050
ACS Sens. 2021, 6, 2553−2562

("microwalk") on the top wall of the chamber and toward the opposite side.[23,24]

Subsequently, when sufficient magnetic beads reach the opposite side, the microwalkers start tumbling on the floor of the microchamber toward the right side of the chamber and so on, reaching a stable circulatory collective motion soon (Figure 5) (video of the side view can be found in Supporting Information Movie S3.5). As long as the rotating field is applied, the MPS steadily continues and even though the details of individual magnetic beads continuously change, the collective swarming behavior remains stable in time. It is also noted that inertia does not play a role in this type of actuation as the MPS and overall SPIOM motion stopped immediately when the magnetic field was switched off, apart from the particles sedimenting due to gravity (Supporting Information Movie S3.8). Remarkably, the global circulatory motion is opposite to the rotational directions of the particle beads and clusters: whereas the latter rotate clockwise, with the magnetic field rotation, the former is counterclockwise, against the magnetic field rotation. As a result, the beads also induce fluid flows with opposing directionalities. The combination of these two counteracting flows, that is, local clockwise vortices due to rotating chains and clusters and global vortical flow due to the surface microwalkers, is expected to give rise to an enhanced global mixing effect and subsequently fast and good mixture quality (sample homogeneity).

From Figure 4, a clear correlation emerges between the Mason number and MPS: with a few exceptions, swarming is only observed for Mason numbers between 0.1 and 2. Hence, the ratio of viscous to magnetic forces (and torques) is a main determinant for swarming to occur, as also suggested above in the qualitative description of the mechanism involved in generating swarming. If *Ma* is too large (>2), viscous drag forces dominate, chains break up, and the particles cannot escape from the magnetic gradient force at the chamber edge. For very small *Ma* (<0.1), the rotational speed of the bead chains is too low to generate sufficient flow to overcome the magnetic gradient force toward the microchamber edge, and they are trapped within the island observed near the edge as well (such as in Figure 3, top-row images).

FLOW KINETICS INDUCED BY VARIOUS MIXING CONDITIONS: MPS AND ITS EFFECT ON MIXING

The motion of magnetic particles does not necessarily represent the induced flow. To investigate this relation, the fluid flow caused by particle actuation with the vertical rotational magnetic field is visualized by using 3D-particle tracking velocimetry (3D-PTV) based on the general defocusing particle tracking method (see also Supporting Information Text S4).[25] Figure 6 shows the mean velocity profiles as a function of the vertical position in the chamber, from bottom to top, in different mixing conditions. The colors of the trajectories designate the direction of the horizontal-velocity component. There is a clear bias for a positive horizontal velocity near the bottom and a clear bias for a negative horizontal velocity near the top of the fluid chamber, which is in accordance with the clockwise global circulation of the magnetic particles.

In the absence of actuation (Figure 6a), the velocity is minimal, limited to less than 1 μm s^{-1}, so convection is practically absent. For the case in which actuation is applied, but where no swarming is observed, shown in Figure 6b, fluid kinetics are introduced and significant flow velocities are measured with a positive direction in the lower half of the channel, with a maximum of 100 μm s^{-1}. Figure 6c shows that MPS significantly enhances the horizontal fluid velocity, with a maximum value of 500 μm s^{-1}. In addition, the mean velocity is positive (to the right) in the lower half of the chamber and negative (to the left) in the upper half, while the profile is mostly symmetric with respect to the channel midplane at z = 250 μm.

This is consistent with counterclockwise global circulatory fluid flow, suggesting that the flow is driven by the global counterclockwise motion of the magnetic particles observed in the previous section. Figure 6d shows the root-mean-square (rms) of both the horizontal velocity component V_x and V_y derived from the trajectories, being a measure for the level of fluid velocity fluctuations—likely being important for mixing. The rms is small for V_y, but substantially larger for V_x. Also, as expected for magnetic fields strengths corresponding to MPS (i.e., 25 mT and higher), the rms of V_x is significantly enhanced.

The mixing performance of the magnetic particle actuation is investigated by observing and analyzing the distribution of fluorescent particles throughout the microfluidic chamber over time. The "intensity of segregation" is widely used as a measure to quantitatively assess mixing performance assessments[26,27] and is chosen here to quantify the mixing index (MI); the procedure is explained in detail in the Supporting Information Texts S1 and S5. Figure 7 shows the results of the normalized

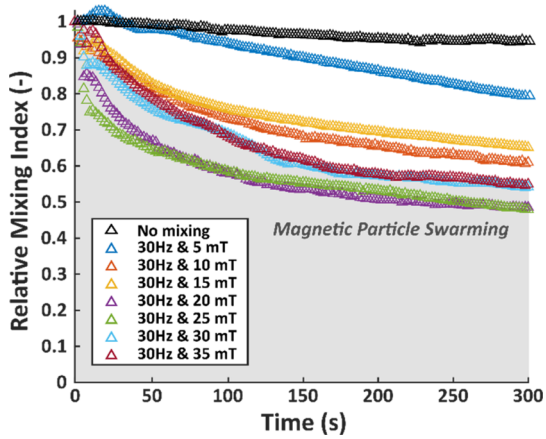

Figure 7. Mixing performance as a function of frequency in a 5 min rotational magnetic actuation protocol. MPS is observed at magnetic field strengths ≥20 mT (gray highlighted area).

version of the MI and the relative MI measurement over time at different actuation conditions. In short, a lower relative MI corresponds to better mixing. All actuation protocols result in an enhancement of mixing compared to the nonactuated control case.

There is a direct link between magnetic field strength and mixing efficiency (the measure of the level of sample homogeneity). Not only is this link observed for the maximum mixing performance achieved but also the time at which that was obtained, that is, the mixing rate (Table 1). The best mixing efficiency is achieved at magnetic field strengths ≥20 mT, which corresponds to a relative MI ≈ 0.5 and at the fastest mixing rates, which coincide with the formation of MPS (as seen in Figure 3). Interestingly, strong magnetic field gradients

https://doi.org/10.1021/acssensors.1c00050
ACS Sens. 2021, 6, 2553−2562

Table 1. Time to Reach MIs for Different Magnetic Field Strengths; MPS Occurs in the Gray Fields

Time to reach Mixing Indexes for Magnetic field strengths [s]				
	Relative Mixing Index [-]			
Magnetic field strength [mT]	0.8	0.7	0.6	0.5
5	276	-	-	-
10	60	132	-	-
15	68	192	-	-
20	20	40	88	232
25	8	28	88	262
30	38	98	158	-
35	50	96	169	-

at magnetic field strengths >30 mT (insert in Figure 3) have a slightly negative effect on the mixing efficiencies.

PILOT STUDY ON THE EFFECT OF SAMPLE HOMOGENEITY ON THE EFFICIENCY OF A BIOLUMINESCENT SENSOR ASSAY

The investigation of the effect of mixing on a bioluminescent sensor entails the comparison of situations of an unmixed (MI_{min} = 0.8, no magnetic actuation was applied), a poorly mixed (MI_{min} = 0.7, 15 mT, 30 Hz, no MPS) and a better-mixed actuation protocol (MI_{min} = 0.6, 35 mT, 30 Hz, MPS) with respect to the efficiency and time to read out of the sensor. Our hypothesis is that good mixing will enhance the kinetics of the sensor−substrate and sensor−AB binding events, which will lead to faster sensor readout. Recently, the local effects of magnetic particle microspinning to protein−protein interactions were studied and the reaction efficiency was increased by 55% at 120 rpm.[28] Here, the MPS adds global phenomena that enhance fluid mixing, and the question is whether this effect is beneficial for accelerating biochemical sensing as well.

AB testing commonly involves two parts: the (bio)chemical sensor and the target (e.g., AB to be detected). The capturing/binding of these two elements may cause a signal to be produced, for example, emitted light, which can then be detected with electronic components and translated into a readout. The sensor of choice is the LUMABS; LUMinescent AB Sensor) that allows AB detection directly in blood plasma. LUMABS is based on bioluminescence resonance energy transfer (BRET) (Figure 8a) that currently allows the detection of antibodies against HIV1-p17, hemagglutinin, and dengue virus type I,[29] while assays for other markers are in development. LUMABS is a single-protein sensor that consists of the blue-light emitting luciferase NanoLuc connected via a semiflexible linker to the green fluorescent acceptor protein mNeonGreen, which are kept close together using helper domains, hence emitting green light. Binding of an AB to epitope sequences flanking the linker disrupts the interaction between the helper domains, resulting in a large decrease in BRET efficiency (Figure 8a); hence, blue emission is enhanced. The ratio of green to blue quantifies the amount (or concentration) of the AB.

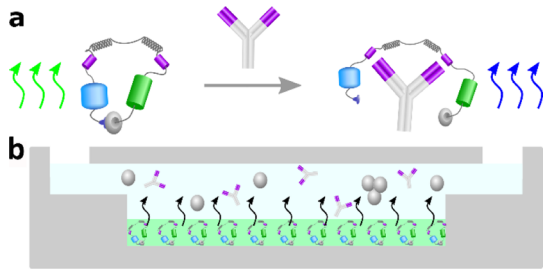

Figure 8. LUMABS sensor. (a) Schematic view of the LUMABS in the absence and presence of a corresponding AB and (b) side view of the chip. The sensor is deposited (dried) on the microfluidic chamber floor. The black arrows depict the transfer of the sensor to the sample by diffusion and/or convection.

To best mimic PoC devices where most of the components are already incorporated inside a cartridge for user-friendliness, the LUMABS is dried in a glycerol matrix inside the microfluidic chip (Figure 8b). The rest of the components such as the magnetic beads, the AB (in our case CTX-2), and the fuel of the sensor and the substrate are added next (for details, see Supporting Information Text S1 "Materials and Methods"). The obtained mages are shown in Figure 9 for the three mixing protocols, and Figure 10 shows the intensity ratio between the green and blue images with time, indicating the speed of detection.

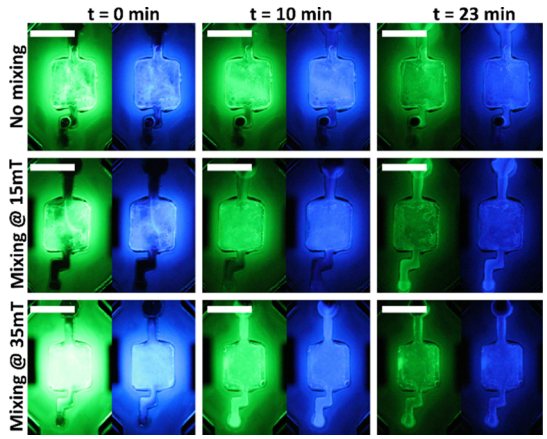

Figure 9. Results of the sensor behavior. The LUMABS sensor is deposited on the floor of a microfluidic chamber, and the sample containing the magnetic beads, the target protein, and substrate molecules is entered into the chamber. Three different states are applied: no actuation/mixing, actuation at 15 mT, in which poor mixing and no MPS is observed, and actuation at 35 mT with better mixing and MPS. Inhomogeneity was reduced by mixing, and the change in color is faster and larger in the mixed states. The magnetic rotational frequency is 30 Hz, the AB concentration is 1.1 μM, and the sensor concentration is 110 nM. Scale bar is 4 mm. See also movies in Supporting Information S6.

Fluid kinetics are expected to play an essential role in the assay. The two interactions required to ensure sensor efficiency are (1) the interaction between the sensor and the substrate molecule and (2) the AB−sensor binding events. In time, the two intensities of green and blue light change due to these events. In a state where no fluid perturbations are introduced (Figure 9, no mixing state), these two interactions are rather slow, as diffusion by Brownian motion causes the predominant molecular motion.

When fluid kinetics are introduced due to the movement of the magnetic beads as actuated by the magnetic protocols (actuation at 30 Hz, 15 mT and 30 Hz, 35 mT), these events

https://doi.org/10.1021/acssensors.1c00050
ACS Sens. 2021, 6, 2553−2562

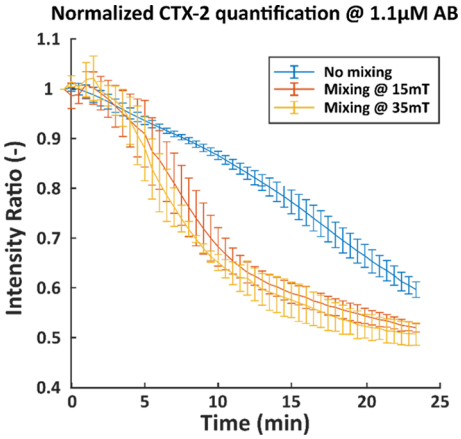

Figure 10. Normalized intensity ratios of the CTX-2 AB. The LUMABs concentration in the fluid chamber is 110 nM, and the AB concentration is at a 10:1 AB sensor ratio. Mixing occurs at 30 Hz magnetic rotational frequency for both 15 and 35 mT.

occur faster, and this is confirmed by the faster color change observed in Figure 9 at 15 mT and mixing at 35 mT.

What is most relevant to the assay is how the ratio of green to blue intensities changes. From Figure 10, it can clearly be seen that both mixing protocols substantially enhance the assay; in particular, the time to readout is faster. The nonmixed state requires 23′ to reach the minimum intensity ratio of 0.6, while this time is halved at the mixed states (14′ at 15 mT and 12.5′ at 35 mT). There is, however, no significant difference between the MPS and the non-MPS protocol, although MPS tends to initially speed up the assay somewhat.

For PoC applications, the total assay time is relevant, and the requirement is typically set at 10 min. The read-out signal at 10 min, represented by the intensity ratio, is significantly enhanced by both mixing scenarios. At 10 min, the no-mixing state portrays an intensity ratio of 0.86, while the mixing at applied 15 mT lowers this value to 0.68 and at applied 35 mT, it is 0.65.

It can be concluded that for the AB sensor studied herein, the introduction of kinetics significantly contributes to a faster readout in excess AB.

CONCLUSIONS

Our results show that magnetic particle actuation, and in particular, the MPS we could generate, has great potential to introduce strong fluid velocities and enhanced mixing in microfluidic reaction chambers. This potentially enhances the operation for applications where sample homogeneity is required in microreaction chambers with initially stagnant fluids, for which passive micromixing strategies do not work. Indeed, we observed that magnetic particle mixing substantially accelerates a bioluminescent PoC assay for the detection of antibodies as compared to the nonactuated diffusion-only case. For the particular assay used, however, the enhanced mixing by MPS only gave a limited additional effect over conventional magnetic bead mixing. How essential MPS is for achieving fast AB detection depends on more factors such as the details of the biochemical reaction kinetics involved, that is, the specific assay used, as well as reagent and target concentrations. It will be interesting to study these effects in future studies.

MPS occurred at certain magnetic field strengths and rotations. To better understand the mechanisms of MPS formation and subsequent effect on sample homogeneity, other parameters should also be varied, such as magnetic bead size, bead magnetic properties, and magnetic bead concentration, and also initial distribution of the magnetic beads on the microfluidic chamber floor. What is more, the rheology of the fluid plays a highly important role for MPS and also for practical applications (e.g., mixing in commercial capillary filling PoC platforms). Overall, MPS offers a general tool to overcome slow diffusion-based water-like mixtures by introducing a straightforward technique to induce global mixing.

ASSOCIATED CONTENT

Supporting Information

The Supporting Information is available free of charge at https://pubs.acs.org/doi/10.1021/acssensors.1c00050.

Materials and methods including magnetic beads and electromagnets, hysteresis loop of the magnetic beads, MI methods and determination, and LUMABS sensor, and forces at play in the magnetic bead motion in the fluid (PDF)

Global magnetic bead behavior in a clockwise vertical rotating magnetic field at 1Hz, 25mT as recorded real-time (MP4)

Global magnetic bead behavior in a clockwise vertical rotating magnetic field at 10Hz, 25mT as recorded real-time (MP4)

Global magnetic bead behavior in a clockwise vertical rotating magnetic field at 30Hz, 25mT as recorded real-time (MP4)

Global magnetic bead behavior in a clockwise vertical rotating magnetic field at 60 Hz, 25mT as recorded real-time (MP4)

Side view of the magnetic particle swarming at 35mT, 30Hz (MP4)

Local dynamics in particle−particle interactions at 35mT, 1Hz (MP4)

Local dynamics in particle−particle interactions and chain breakup and reformation at 35mT, 1Hz (MP4)

Sedimentation of the magnetic beads as soon as the magnetic field is switched off during magnetic particle swarming at 35mT and 30 Hz (MP4)

Real-time mixing efficiency evolution over time on control (MP4)

Mixing efficiency evolution over time on magnetic bead behavior at 15mT, 30Hz (MP4)

Real-time mixing efficiency evolution over time on magnetic bead behavior at 15mT, 30Hz (MP4)

Real-time mixing efficiency evolution over time on magnetic bead behavior at 35mT, 30Hz (AVI)

Sensor behavior in the non-mixed state in a 24-min protocol of antibody concentration at 1.1μM in a 24-min protocol (AVI)

Sensor behavior in the mixing state occurring at 15mT, 30Hz in a 24-min protocol of antibody concentration at 1.1μM (AVI)

Sensor behavior in the mixing state occurring at 35mT, 30Hz with the MPS in a 24-min protocol of antibody concentration at 1.1μM (AVI)

https://doi.org/10.1021/acssensors.1c00050
ACS Sens. 2021, 6, 2553−2562

AUTHOR INFORMATION

Corresponding Author

Jaap den Toonder − *Microsystems Research Section, Department of Mechanical Engineering, and Institute for Complex Molecular Systems (ICMS), Eindhoven University of Technology, Eindhoven 5600MB, The Netherlands*; Email: J.M.J.d.Toonder@tue.nl

Authors

Eriola-Sophia Shanko − *Microsystems Research Section, Department of Mechanical Engineering, and Institute for Complex Molecular Systems (ICMS), Eindhoven University of Technology, Eindhoven 5600MB, The Netherlands*; orcid.org/0000-0002-7674-3893

Lennard Ceelen − *Microsystems Research Section, Department of Mechanical Engineering, Eindhoven University of Technology, Eindhoven 5600MB, The Netherlands*

Ye Wang − *Microsystems Research Section, Department of Mechanical Engineering, and Institute for Complex Molecular Systems (ICMS), Eindhoven University of Technology, Eindhoven 5600MB, The Netherlands*

Yoeri van de Burgt − *Microsystems Research Section, Department of Mechanical Engineering, and Institute for Complex Molecular Systems (ICMS), Eindhoven University of Technology, Eindhoven 5600MB, The Netherlands*; orcid.org/0000-0003-3472-0148

Complete contact information is available at: https://pubs.acs.org/10.1021/acssensors.1c00050

Author Contributions

J.d.T. conceived and supervised the research. E.-S.S. performed all the experimental work and covered the data analysis for the application experiments (LUMABS). L.C. developed the algorithm for the MI quantification and adapted the 3D particle tracking velocimetry data analysis. The sensor was provided by Eva van Aalen, and the results were discussed with Yan Ni. Y.v.d.B., Y.W., and J.d.T. contributed to the discussion of the results and writing the article.

Funding

This research was financially supported by "Toeslag voor Topconsortia voor Kennis en lnnovatie (TKl)" of the ministry of Economic Affairs of the Netherlands, grant no. 16.1049.

Notes

The authors declare no competing financial interest.

ACKNOWLEDGMENTS

The authors would like to thank Erik Homburg for his valuable help with the setup for the LUMABS and Yan Ni and Eva van Aalen for the discussion and provision of the LUMABS sensor.

REFERENCES

(1) Patel, R.; Babady, E.; Theel, E. S.; Storch, G. A.; Pinsky, B. A.; George, St.K.; Smith, T. C.; Bertuzzi, S. Report from the American Society for Microbiology COVID-19 International Summit, 23 March 2020: Value of Diagnostic Testing for SARS−CoV-2/COVID-19. *mBio* **2020**, *11*, No. e00722-20.

(2) Petherick, A. Developing antibody tests for SARS-CoV-2. *Lancet* **2020**, *395*, 1101−1102.

(3) Castillo-Torres, K. Y.; McLamore, E. S.; Arnold, D. P. A high-throughput microfluidic magnetic separation (μFMS) platform for water quality monitoring. *Micromachines* **2019**, *11*, 16.

(4) Zhou, Y.; Dong, Z.; Andarge, H.; Li, W.; Pappas, D. Nanoparticle modification of microfluidic cell separation for cancer cell detection and isolation. *Analyst* **2020**, *145*, 257−267.

(5) Li, F.; Guo, L.; Hu, Y.; Li, Z.; Liu, J.; He, J.; Cui, H. Multiplexed chemiluminescence determination of three acute myocardial infarction biomarkers based on microfluidic paper-based immunodevice dual amplified by multifunctionalized gold nanoparticles. *Talanta* **2020**, *207*, 120346.

(6) Yamaguchi, N.; Fujii, Y. Rapid on-site monitoring of bacteria in freshwater environments using a portable microfluidic counting system. *Biol. Pharm. Bull.* **2020**, *43*, 87−92.

(7) Garcia-Cordero, J. L.; Maerkl, S. J. Microfluidic systems for cancer diagnostics. *Curr. Opin. Biotechnol.* **2020**, *65*, 37−44.

(8) Miller, P. G.; Chen, C. Y.; Wang, Y. I.; Gao, E.; Shuler, M. L. Multiorgan microfluidic platform with breathable lung chamber for inhalation or intravenous drug screening and development. *Biotechnol. Bioeng.* **2020**, *117*, 486−497.

(9) van Reenen, A.; de Jong, A. M.; den Toonder, M. J. Integrated lab-on-chip biosensing systems based on magnetic particle actuation − a comprehensive review. *Lab Chip* **2014**, *14*, 1966.

(10) Shanko, E.-S.; van de Burgt, Y.; Anderson, P. D.; den Toonder, J. M. J. Microfluidic magnetic mixing at low Reynolds numbers and in stagnant fluids. *Micromachines* **2019**, *10*, 731.

(11) Dong, Z.; Delacour, C.; Mc Carogher, K.; Udepurkar, A. P.; Kuhn, S. Continuous Ultrasonic Reactors: Design, Mechanism and Application. *Materials* **2020**, *13*, 344.

(12) Melle, S.; Calderón, O. G.; Rubio, M. A.; Fuller, G. G. Microstructure evolution in magnetorheological suspensions governed by Mason number. *Phys. Rev. E: Stat. Phys., Plasmas, Fluids, Relat. Interdiscip. Top.* **2003**, *68*, 041503.

(13) Gon Kang, T.; Gao, Y.; Hulsen, M. A.; den Toonder, J. M. J.; Anderson, P. D. Direct simulation of the dynamics of two spherical particles actuated magnetically in a viscous fluid. *Comput. Fluids* **2013**, *86*, 569−581.

(14) Gao, Y.; Beerens, J.; van Reenen, A.; Hulsen, M. A.; de Jong, A. M.; Prins, M. W. J.; den Toonder, J. M. J. Strong vortical flows generated by the collective motion of magnetic particle chains rotating in a fluid cell. *Lab Chip* **2015**, *15*, 351−360.

(15) Zhang, S.; Cui, Z.; Wang, Y.; den Toonder, J. M. J. Metachronal actuation of microscopic magnetic artificial cilia generates strong microfluidic pumping. *Lab Chip* **2020**, *20*, 3569−3581.

(16) Gao, Y.; van Reenen, A.; Hulsen, M. A.; de Jong, A. M.; Prins, M. W. J.; den Toonder, J. M. J. Disaggregation of microparticle clusters by induced magnetic dipole−dipole repulsion near a surface. *Lab Chip* **2013**, *13*, 1394.

(17) van Pelt, S.; Frijns, A.; den Toonder, J. Microfluidic magnetic bead conveyor belt. *Lab Chip* **2017**, *17*, 3826−3840.

(18) Rida, A.; Gijs, M. A. M. Manipulation of self-assembled structures of magnetic beads for microfluidic mixing and assaying. *Anal. Chem.* **2004**, *76*, 6239−6246.

(19) Petousis, I.; Homburg, E.; Derks, R.; Dietzel, A. Transient behaviour of magnetic micro-bead chains rotating in a fluid by external fields. *Lab Chip* **2007**, *7*, 1746.

(20) Kang, T. G.; Hulsen, M. A.; Anderson, P. D.; den Toonder, J. M. J.; Meijer, H. E. H. Chaotic mixing induced by a magnetic chain in a rotating magnetic field. *Phys. Rev. E: Stat., Nonlinear, Soft Matter Phys.* **2007**, *76*, 066303.

(21) Kokot, G.; Snezhko, A. Manipulation of emergent vortices in swarms of magnetic rollers. *Nat. Commun.* **2018**, *9*, 2344.

(22) Yu, J.; Yang, L.; Zhang, L. Pattern generation and motion control of a vortex-like paramagnetic nanoparticle swarm. *Int. J. Microbiol. Res.* **2018**, *37*, 912−930.

(23) Morimoto, H.; Ukai, T.; Nagaoka, Y.; Grobert, N.; Maekawa, T. Tumbling motion of magnetic particles on a magnetic substrate induced by a rotational magnetic field. *Phys. Rev. E: Stat., Nonlinear, Soft Matter Phys.* **2008**, *78*, 021403.

(24) Sing, C. E.; Schmid, L.; Schneider, M. F.; Franke, T.; Alexander-Katz, A. Controlled surface-induced flows from the motion

of self-assembled colloidal walkers. *Proc. Natl. Acad. Sci. U.S.A.* **2010**, *107*, 535−540.
(25) Barnkob, R.; Kähler, C. J.; Rossi, M. General defocusing particle tracking. *Lab Chip* **2015**, *15*, 3556−3560.
(26) Raza, W.; Hossain, S.; Kim, K.-Y. Effective mixing in a short serpentine split-and-recombination micromixer. *Sens. Actuators, B* **2018**, *258*, 381−392.
(27) Lu, L.-H.; Ryu, K. S.; Liu, C. A magnetic microstirrer and array for microfluidic mixing. *J. Microelectromech. Syst.* **2002**, *11*, 462−469.
(28) Kim, S. D.; Song, S. W.; Oh, D. Y.; Lee, A. C.; Koo, J. W.; Kang, T.; Kim, M. C.; Lee, C.; Jeong, Y.; Jeong, H. Y.; Lee, D.; Cho, S.; Kwon, S.; Kim, J. Microspinning: local surface mixing via rotation of magnetic microparticles for efficient small-volume bioassays. *Micromachines* **2020**, *11*, 175.
(29) Arts, R.; den Hartog, I.; Zijlema, S. E.; Thijssen, V.; van der Beelen, S. H. E.; Merkx, M. Detection of Antibodies in Blood Plasma Using Bioluminescent Sensor Proteins and a Smartphone. *Anal. Chem.* **2016**, *88*, 4525−4532.

https://doi.org/10.1021/acssensors.1c00050
ACS Sens. 2021, 6, 2553−2562